Permeability and elastic properties of rocks from the northern Hikurangi margin: Implications for slow-slip events

Nicola Tisato[1], Carolyn D. Bland[1*], Harm Van Avendonk[2], Nathan Bangs[2], Hector Garza[1], Omar Alamoudi[1], Kelly Olsen[2†], Andrew Gase[2‡]

[1] Department of Earth and Planetary Sciences, Jackson School of Geosciences, The University of Texas at Austin, Austin, TX, U.S.

[2] Institute for Geophysics, Jackson School of Geosciences, The University of Texas at Austin, Austin, TX, U.S.

[*] Now at: Pariveda Solutions, Dallas, TX, U.S.

[†] Now at: Descartes Labs, 1607 Paseo de Peralta, Suite B, Sante Fe, NM, U.S.

[‡] Now at: Geology Department, Western Washington University, Bellingham, WA, U.S.

Corresponding author: Nicola Tisato (nicola.tisato@jsg.utexas.edu)

Key Points:

- We studied elastic properties, plastic deformation, and permeability of northern Hikurangi margin rocks
- We provide a permeability-porosity relationship for accretionary prism mudrocks
- Permeability healing in the Hikurangi accretionary prism rocks provides a mechanism justifying slow-slip event cyclicity

Abstract

Fluid flow and pore-pressure cycling are believed to control slow slip events (SSEs), such as those that frequently occur at the northern Hikurangi margin (HM) of New Zealand. To better understand fluid flow in the forearc system we examined the relationship between several physical properties of Cretaceous-to-Pliocene sedimentary rocks from the Raukumara peninsula. We found that the permeability of the deep wedge is too low to drain fluids, but fracturing increases permeability by orders of magnitude, making fracturing key for fluid flow. In weeks to months, plastic deformation, swelling, and possibly not-yet-identified mechanisms heal the fractures, restoring the initial permeability. We conclude that overpressures at the northern HM might partly dissipate during SSEs due to enhanced permeability near faults. However, in the months following an SSE, healing in the prism will lower permeability, forcing pore pressure to rise and a new SSE to occur.

Plain Language Summary

Earth's crust comprises many tectonic plates fitting together like jigsaw puzzle pieces. Tectonic plates subduct in the mantle along active converging margins, where the forces driving such a convergence can trigger large earthquakes. However, these subduction zones often deform without producing earthquakes, but through slow deformations called slow slip events (SSE). The Hikurangi Margin (HM) of New Zealand is a well-studied subduction zone, producing both earthquakes and SSEs. The northern HM exhibits more frequent and shallower SSEs than the southern margin. Understanding what controls such differences can help improve the general understanding of subduction zone mechanics and earthquakes. One of the hypotheses is that the differences between the deformation of the northern and southern HM are controlled by the pressure of fluids at depth. We tested the elastic and fluid-transport properties of four samples from the northern HM and found that the overriding plate, if not fractured, would be impermeable to fluids. We also tested a fractured sample and observed efficient healing that resets the initial permeability. We conclude that fracturing the overriding plate is fundamental to draining the fluids carried at depth by the subducting plate, and SSEs may create new pathways for fluids to escape to the seafloor.

1 Introduction

At the shallow (<15 km depth) portion of the plate interface of subduction zones, scientists have found that convergence between the tectonic plates is often accommodated by modes of slip in between earthquakes and aseismic creep (Saffer & Wallace, 2015). Slow-slip events (SSEs) represent one class of such transient phenomena, which can lead to several centimeters of slip over several days to months (Schwartz & Rokosky, 2007). The relatively large seismic moment released by shallow SSEs, comparable to that of earthquakes (Passarelli et al., 2021), proves the importance to understand SSEs and how they influence the seismogenic character of a convergent margin. Frictional properties and stress heterogeneities along the plate interface might favor SSEs (Barnes et al., 2020; Bell et al., 2010; Boulton et al., 2019; Im et al., 2020; Leah et al., 2022; Rabinowitz et al., 2018; Shreedharan et al., 2023). Moreover, subducting oceanic crust and sediments release large volumes of fluids whose pressure can exceed hydrostatic conditions when confined within low permeability rocks, lowering the effective stress on the shallow megathrust or splay faults and creating conditions conducive to SSEs (Ellis et al., 2015; Kitajima & Saffer, 2012; Tsuji et al., 2008; Warren-Smith et al., 2019).

The northern Hikurangi margin (HM) in New Zealand, is a subduction zone with a shallow forearc and plate interface, where sediment accretion, compaction, and deformation have been modulated for millions of years by underthrusting seamounts (Gase et al., 2021; Sun et al., 2020). Subducting seamounts may cause stress heterogeneities (Bangs et al., 2023; Leah et al., 2022; Sun et al., 2020) and fluid pressure transients (Shaddox & Schwartz, 2019) that can lead to SSEs, several of which have been characterized in great detail by onshore geodetic and offshore absolute pressure gauge (APG) data (Yohler et al., 2019). Offshore Gisborne SSEs occur every 1-2 years and can last several weeks, during which time 5 to 30 cm of slip may be accommodated (Wallace, 2020). Temporal variations in the character of earthquake focal mechanisms within the subducting oceanic crust provide compelling evidence for low effective stress before an SSE (Warren-Smith et al., 2019). This observation suggests that fluid pressure increases enable SSEs and that the slip is accompanied by fluid release. Nevertheless, fluid transport through the accretionary wedge in this deformation cycle is not yet well understood (Antriasian et al., 2018).

The physical properties of accreted sediments of the northern HM and their relationship to slip phenomena have been studied recently using cores and data from IODP expeditions (e.g., Wallace et al., 2019). The resulting studies have shed new light on the frictional properties, shallow dewatering, and faulting near the seafloor (Aretusini et al., 2021; Boulton et al., 2019, 2022; Dutilleul et al., 2021; Fagereng et al., 2019; French & Morgan, 2020; Shreedharan et al., 2022). However, to understand how fluid flow and deformation interplay in the deeper prism, we also must consider the physical properties of older, compacted, and diagenetically mature strata (Bland et al., 2015, Bassett et al., 2022). Here, we present and discuss laboratory testing performed on rock samples from the subaerial northern HM as proxies of deep rocks in the prism to understand fluid transport within the accretionary prism better.

2 Materials and Method

To test the mechanical and transport properties of rocks from the northern HM, we collected and performed experiments on outcrop samples from the Raukumara peninsula (Figs 1,S1) presenting different ages and degrees of diagenesis. In the central part of the peninsula, we collected a very-fine to fine-grained sandstone from the Jurassic-to-Early Cretaceous Torlesse Supergroup forming the backstop for the accretionary wedge (sample MO02) (Adams & Graham, 1996; Mortimer et al., 2014). Just east of sample MO02 location, we sampled a calcareous siltstone to very-fine-grained sandstone from the Late Cretaceous-to-Paleocene Tinui Group (sample MT07) that likely represents an early passive margin deposit, now buried in the accretionary wedge (Mortimer et al., 2014). Closer to the East coast, we collected a siltstone (sample GB13) from the middle Miocene Tolaga Group, which sedimented in slope basins after subduction initiated along the HM (van de Lagemaat et al., 2022), and a glauconitic siltstone (sample FB12) from the Pliocene Mangaheia Group.

We determined mineral abundances and assemblages of each sample through X-ray diffraction (XRD) analyses and transmitted light microscopy by preparing 30 μm-in-thickness thin sections. We prepared cylindrical core plugs with parallel end faces for each sample to estimate density, porosity, compressional and shear ultrasonic wave velocities (i.e., Vp and Vs), and helium gas permeability. Samples were tested for confining pressures (P_c) up to 200 MPa (~12.5 km depth for hydrostatic pore pressure and overburden density of 2.6 g/cm^3) and deviatoric vertical force (F_v) ~2.6 kN. Each core plug was mounted inside a PVC jacket and between two core holders equipped with ultrasonic transducers and fluid ports to saturate and measure the core permeability. This sample assembly is mounted inside the triaxial cell between the load cell and the vertical force piston. We define the mean stress as $\sigma_M = \frac{\sigma_1+\sigma_2+\sigma_3}{3}$, where $\sigma 2 = \sigma 3 = Pc$ and σ_1 is the maximum vertical stress: $\sigma_1 = \sigma_d + P_c$, where $\sigma_d = \frac{F_V}{A}$ is the deviatoric stress, and A is the sectional area of the core plug. We also define effective stress (σ') as the difference between the mean stress and the pore pressure: $\sigma' = \sigma_M - P_p$.

We measured ultrasonic velocities using the transmission method at room temperature and a frequency of ~800 kHz (Birch, 1960). To understand the effect of saturation on *V*p and *V*s, we measured the ultrasonic velocities of sample GB13 saturated with water previously chemically equilibrated with the sample. During 30 hours, we recorded the injection of 4.7 ml of this fluid, equivalent to 136% of GB13 pore-space volume.

Sample permeabilities were calculated through the transient method, measuring the pressure equilibration of the helium gas contained in two volumes connected to the sample end-faces and flowing through the sample (Sutherland & Cave, 1980). To understand the effect of porosity reduction on the permeability of young, loosely consolidated rocks, we assumed FB12 isotropic and measured its permeability during mechanical compaction. First, we measured ultrasonic velocities and permeabilities at P_c up to 70 MPa and σ_d=5 MPa, then, we increased P_c stepwise to 100, 150 and 200 MPa and waited for 19, 24 and 5 hours to measure creep until the observed shortening rate was less than 1 μm/hour. Finally, we measured permeability for P_c up to 200 MPa.

To study how fractures influence the permeability of HM rocks, we split sample MT07 through a Brazilian test producing a sub-vertical fracture connecting the opposite end-faces of the core plug. Then, to study the effect of stress on permeability healing, we kept the sample dry and measured permeability as a function of σ', and we collected three micro-computed tomographies (μCT) to seek evidence of variations in fracture aperture. A detailed chronology of the operations follows: On day 1, after the Brazilian test, we collected μCT dataset S1. Between day 2 and 9 we performed the first permeability test (kT1) for σ' between 24 and 65 MPa. During kT1 (days 3 to 5) we promoted healing by keeping σ' to 65 MPa. After kT1 and for the next 39 days, the sample remained inside the pressure vessel at σ'~0 MPa. Between day 48 and day 77, we performed the second permeability test (kT2) at σ' ranging 5.6 to 64 MPa. At the end of kT2 we removed the sample from the pressure vessel and acquired μCT dataset S2. Then, the jacketed sample was placed inside a humidity-controlled chamber equipped with a water container and a thermo-hygrometer. For 72 hours, a medium to low vacuum (<0.5 bar) was maintained to promote water evaporation, causing the chamber relative humidity to remain above 97% and activating minerals (e.g., clays and carbonates) with pronounced swelling or dissolution/precipitation properties (Villar et al., 2005). Finally, we acquired μCT dataset S3, and produced a thin section perpendicular to the sample axis, on which we examined the morphology of the fracture for evidence of clay infilling, possibly caused by plastic deformation and triggered by clay swelling.

Each μCT dataset comprises 1600, 33.3 μm resolution, 16-bits TIFF images perpendicular to the sample axis, recording the entire sample except 4.37 mm at the top and bottom. After normalization and segmentation, we calculated fracture apertures (B) for each CT dataset by producing fracture aperture distribution projections (FADP) whose mean and standard deviation provided average apertures (B_m) and associated uncertainties. We report more details on the methods in the supporting information.

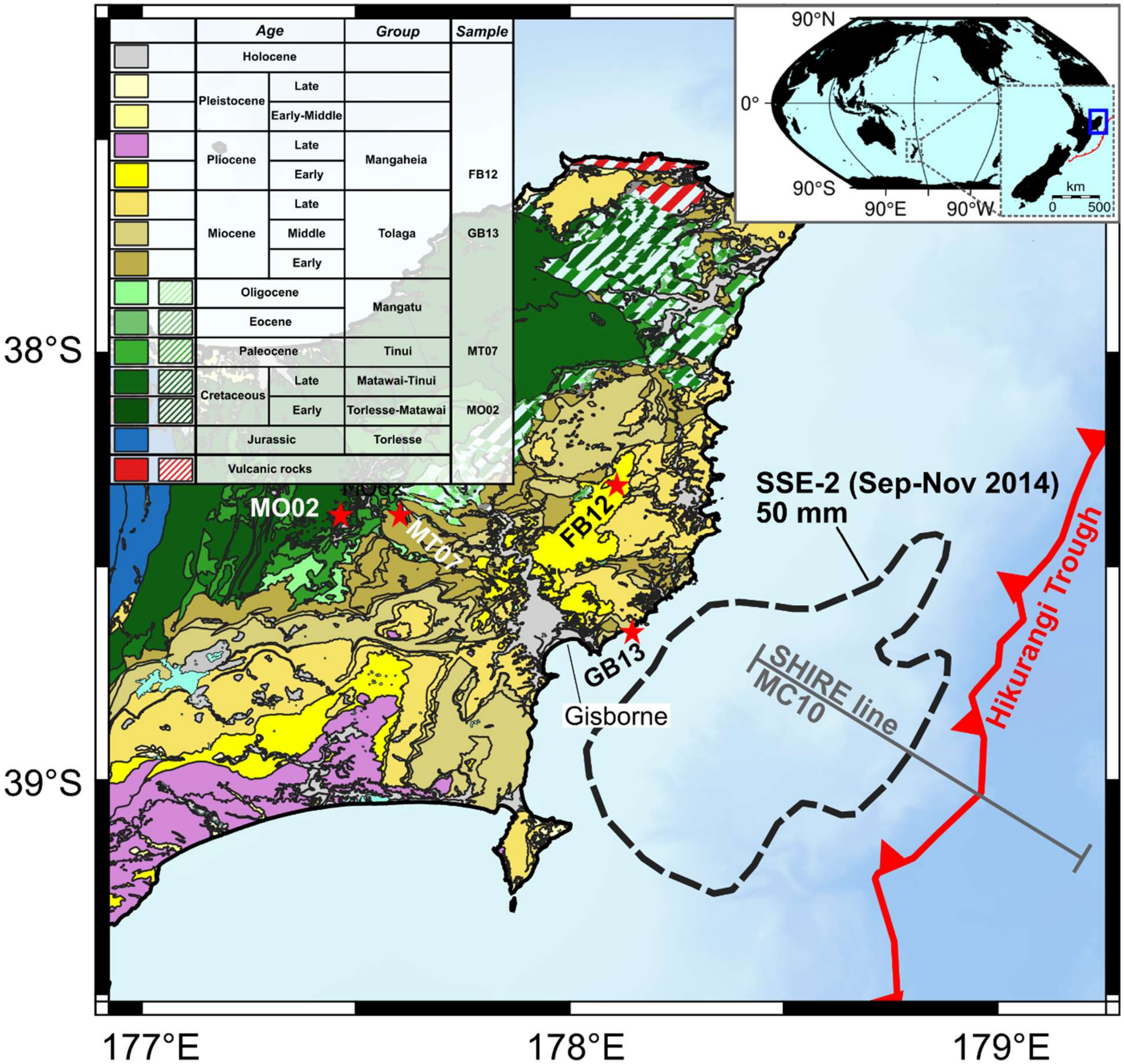

Figure 1. Geologic map of the Raukumara peninsula with the position of our rock samples (Mazengarb & Speden, 2000). The offshore dashed line contour marks the 50 mm geodetic slip model for the September-November 2014 SSE (Warren-Smith et al., 2019). The offshore line indicates the SHIRE project seismic line MC10 (Gase et al., 2021).

3 Results

The four samples contain more than 35 wt% quartz and feldspars. The remaining minerals are calcite, and clays, of which mica, illites and smectites group minerals (swelling clays) represent at least 13 wt%, while kaolinite and chlorite is up to 5 wt% (Figs S1, S2, S3). Porosities vary between 7 and 18%, where the tighter samples (MT07 and MO02) have a longer diagenetic or metamorphic history. Photomicrographs reveal that the grain size varies significantly among the four samples, except for MO02, the large majority of the grains have size <63 μm, suggesting that our samples are siltstones (i.e., mudrocks) to fine grain sandstones in agreement with the regional geology (Mazengarb & Speden, 2000).

Ultrasonic velocity measurements (Fig 2A) show that Vp and Vs increase with σ_m, and the younger samples (FB12 and GB13) generally have lower velocities. Vp to Vs ratios vary between 1.65 and 1.9, with the least consolidated and youngest sample (FB12) exhibiting the highest values. After saturation, sample GB13 Vp increased by ~250 m/s on average while Vs decreased by ~100 m/s on average, increasing the Vp to Vs ratio from ~1.65 to ~1.9.

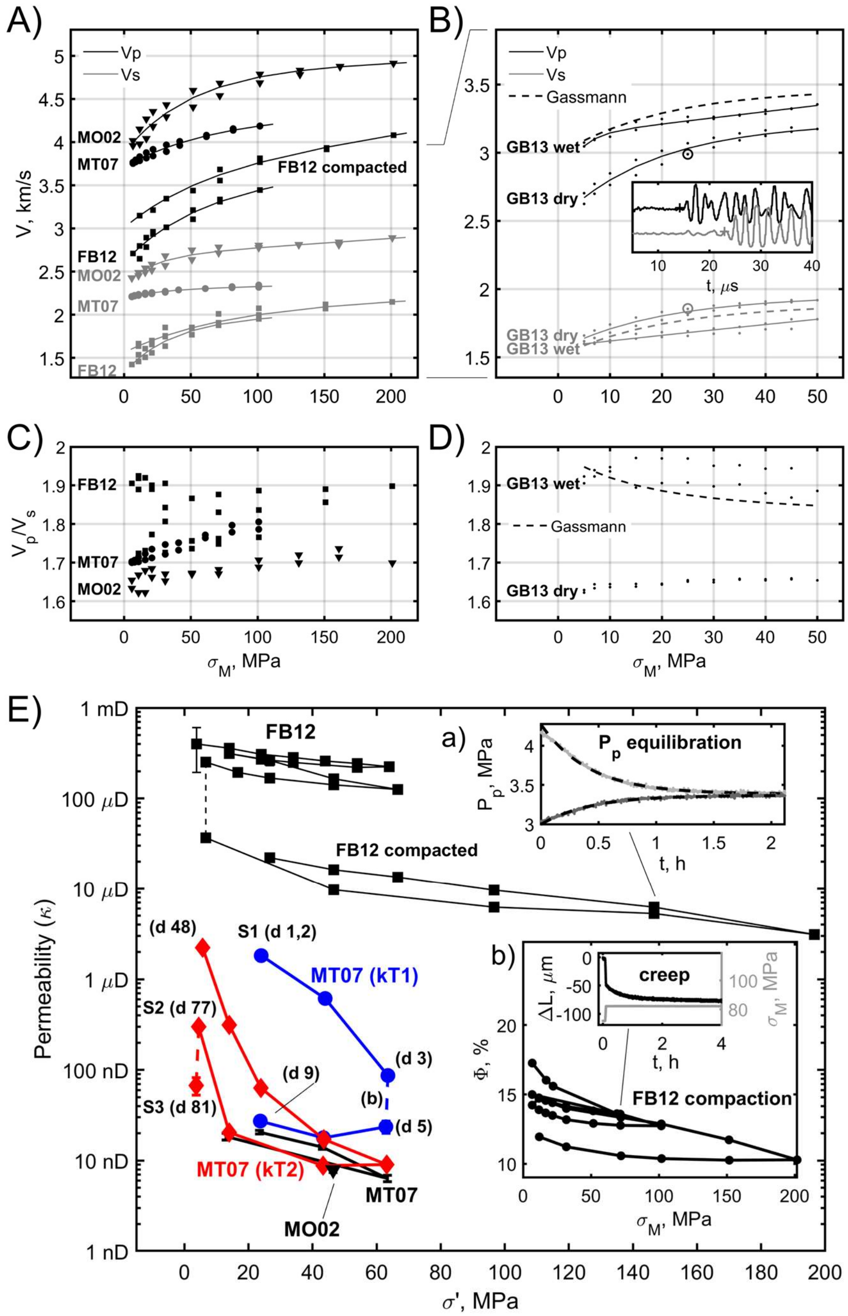

Figure 2. A) Ultrasonic velocities measured on the samples MO02, MT07 and FB12 as a function of σ_M. B) Ultrasonic velocities for dry and water saturated GB13 sample. Dashed lines indicate the theoretical saturated velocities from Gassmann fluid substitution (Gassmann, 1951). Inset: examples of P and S waveforms recorded at the conditions indicated by the circled dots. C and D) Vp to Vs ratios for the laboratory data and the fitting curves reported in A and B, respectively. E) Permeabilities for samples FB12, MT07, and MO02 as a function of σ'. The blue and red curves show the permeability of sample MT07 after fracturing and during two measurement cycles (kT1 and kT2): (d X) near data points indicates X days since stage S1, when the sample was CT-scanned (Fig 3A). After kT1 and

kT2, on day 77 is stage S2 when the sample was CT-scanned again and exposed to a humid atmosphere for 72 hours(Fig 3B). Day 81 was stage S3 and the sample was CT-scanned and re-tested for permeability (Fig 3C,D,E). a) Example of pore pressure (Pp) equilibration and fitting curves (dashed lines) for the indicated permeability datapoint. b) Sample FB12 loss of porosity due to the increase of σ_M. Inset: example of partial compaction due to creep after a σ_M increase.

Before compaction, sample FB12 permeability ranged between 200 and 400 μD. Then, we raised P_c twice to 70 MPa, causing the permeability to decrease by a factor of two and porosity by 3% (i.e., at σ_m~7 MPa, porosity varied from 17.3 to 14.2%). In the following two cycles, where P_c reached 200 MPa, porosity decreased to 13.9%, and the permeability declined by almost an order of magnitude. Concurrently, the ultrasonic Vp increased from 2.6 km/s to 4 km/s.

Samples MO02 and MT07, when intact, have permeabilities below 100 nD, regardless of σ'. The permeability of the fractured MT07 evolved between stages S1, S2, and S3. After S1 and during the permeability cycle kT1, the permeability dropped from 2 to 0.087 μD . After exposing the sample to σ'~65 MPa for more than 48 hours (Fig 4B b), we continued kT1 and found that the permeability further decreased to 24 nD. The permeability remained ~2 orders of magnitude lower than the initial permeability, i.e., around 30 nD, when σ' was reduced. After 39 days, the new increase of σ' during the second permeability cycle kT2, caused the permeability to drop to 9 nD. During the following decrease of σ', the permeability resembled pre-fracturing values. The last measurement of kT2 was performed at σ'=4.5 MPa and permeability was 300 nD, seven times lower than the initial value measured at σ'=5.6 MPa. After exposing the sample to humidity for 72 hours, the permeability, measured at σ'=3.7 MPa, decreased to 67 nD.

Visual inspection and analyses on CT-scans reveal that B_m varied from 190+/-110 μm, to 72+/-43 μm and 84+/-45 μm during stages S1, S2, and S3, respectively (Fig 3A,B,C). During the same stages, the number of voxels counted within the fracture varied from ~934,000 to ~581,000 and ~797,000. Photomicrographs of sample MT07 at stage S3 show that in several loci, the fracture collapsed, and a fine-grained amorphous mass infilled the fracture (Fig 3D,E). These observations suggest that varying confining pressure and humidification caused plastic deformation of clay minerals and swelling, partially closing the fracture and reducing the permeability.

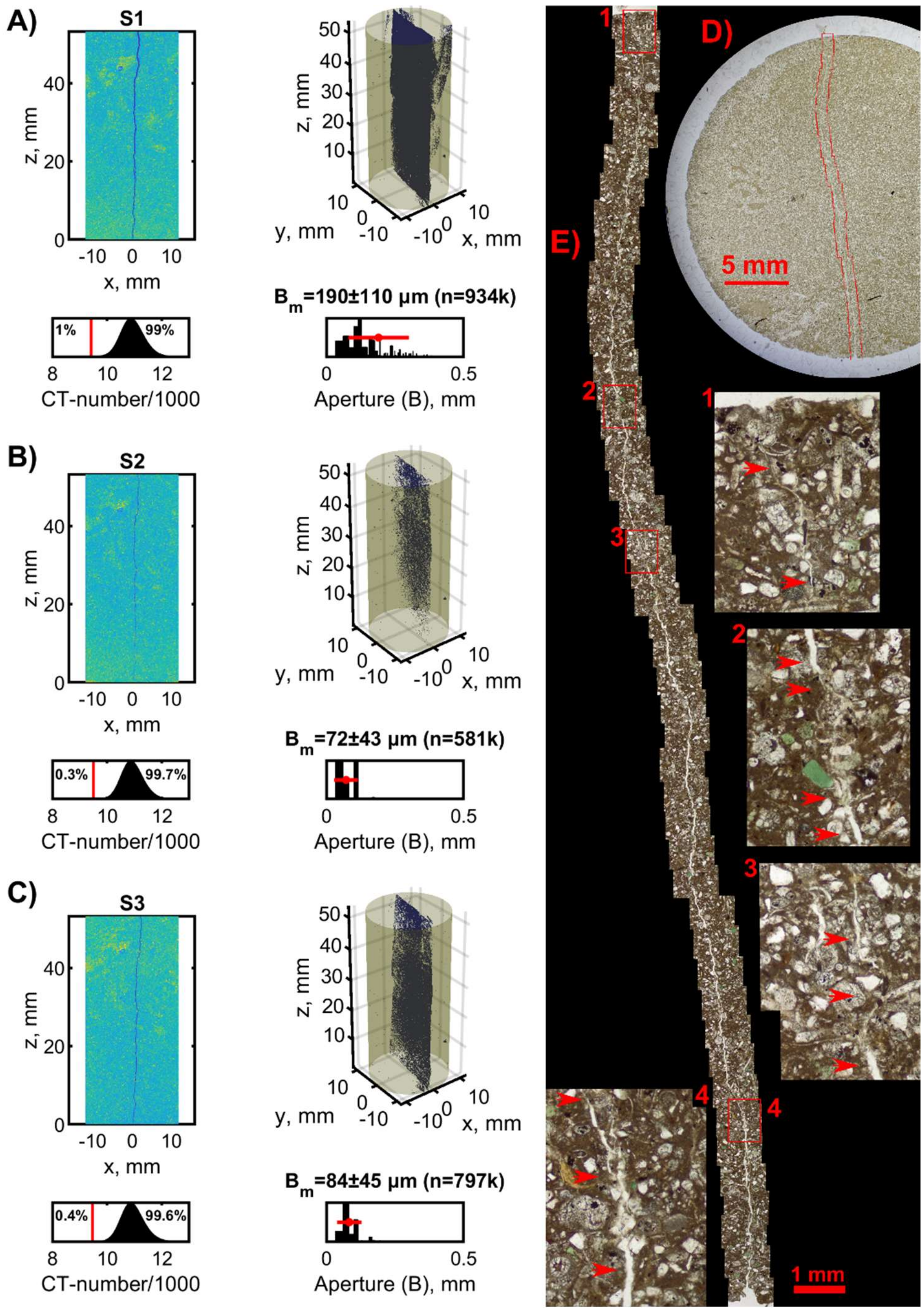

Figure 3. CT-scan and photomicrographs of sample MT07 after fracturing. A, B, and C are CT-scans at stages S1, S2, and S3, respectively. Top-left insets report the vertical section of the CT-scan model after normalization (fig. S4). CT-number distribution is shown in the bottom-left inset. The red vertical line indicates t_x (eq. S5) and the percentages indicate the relative quantity of voxels representing air (on the left) and solid rock (on the right), respectively. The right top inset in each panel shows the binarized 3D model, where voxels within the fracture are blue. The bottom right insets show the aperture distribution (B), the calculated average and standard deviation (B_m and horizontal red bar), and the total count of voxel within the fracture (n). Panel D is a photomicrograph of the thin section at stage S3.

Panel E reports zooms from panel D. Insets 1 to 4 show fracture infill, which are highlighted by red arrows along with open fractures. Panel E original image is included in the data repository (resolution=0.31μm/pixel).

4 Discussion

We provide porosity-permeability relationships for rock samples from the subaerial northern HM under various confining pressures. Ultrasonic velocities of dry samples are similar to the seismic velocities estimated offshore New Zealand by the SHIRE project (Gase et al., 2021). The seismic reflectivity imaged along the transect MC10 shows the décollement and several splay faults that may partly accommodate the convergence (Fig 4A). Inside the prism, Vp increases from 2.0 km/s near the surface to 4.5 km/s at the prism base ~7 km below sea level. The comparison between the seismic and ultrasonic velocities (Fig 4B) suggests that sample FB12 and possibly sample GB13 represent the modern slope basins on the outer prism, consistent with their depositional environment. Deeper in the prism, Vp reaches 4.5 km/s as compaction and diagenesis must have hardened the rock (Dvorkin & Nur, 1996; Saxena & Mavko, 2014). The ultrasonic velocities of the Tinui group sample (MT07) correspond well to the velocities of the deep part of the prism, which is in agreement with the idea that these Paleocene rocks form the base of the prism (Mazengarb & Speden, 2000; Nicol et al., 2007). At 150 MPa (~7 km depth), the ultrasonic Vp of the Torlesse sample (MO02) is 4.8 km/s, which is higher than what we imaged in the deep prism on Line MC10 (Fig 4), suggesting that there may not be a deep offshore portion of the Torlesse basement offshore northern HM (Bassett et al., 2022; Gase et al., 2021).

The seismic to ultrasonic velocities comparison (Fig. 4) is semi-quantitative as uncertainty is introduced by frequency differences and microcracks produced during sample preparation (Eberhart-Phillips et al., 1989; Tsuji & Iturrino, 2008). Velocities in section MC10 and our samples have been measured at frequencies around 20 and 800,000 Hz, respectively. Considering the frequency range, a typical P-wave quality factor between 30 and 150, and a nearly-constant Q model (Liu et al., 1976; Tisato et al., 2021), we should expect velocity dispersion between 2.3 and 12%. Conversely, SHIRE and laboratory data were collected on saturated and dry samples, respectively. Saturation increases P-wave velocities of sample GB13 by ~10%, suggesting that the effect of fluid saturation and anelasticity on velocities should counteract each other. Given the similarity in P-wave velocities and depositional environment, we suggest that the Tinui and Tolaga group rocks (MT07 and GB13) are good lithological proxies for the deep and shallow offshore Hikurangi prism, respectively.

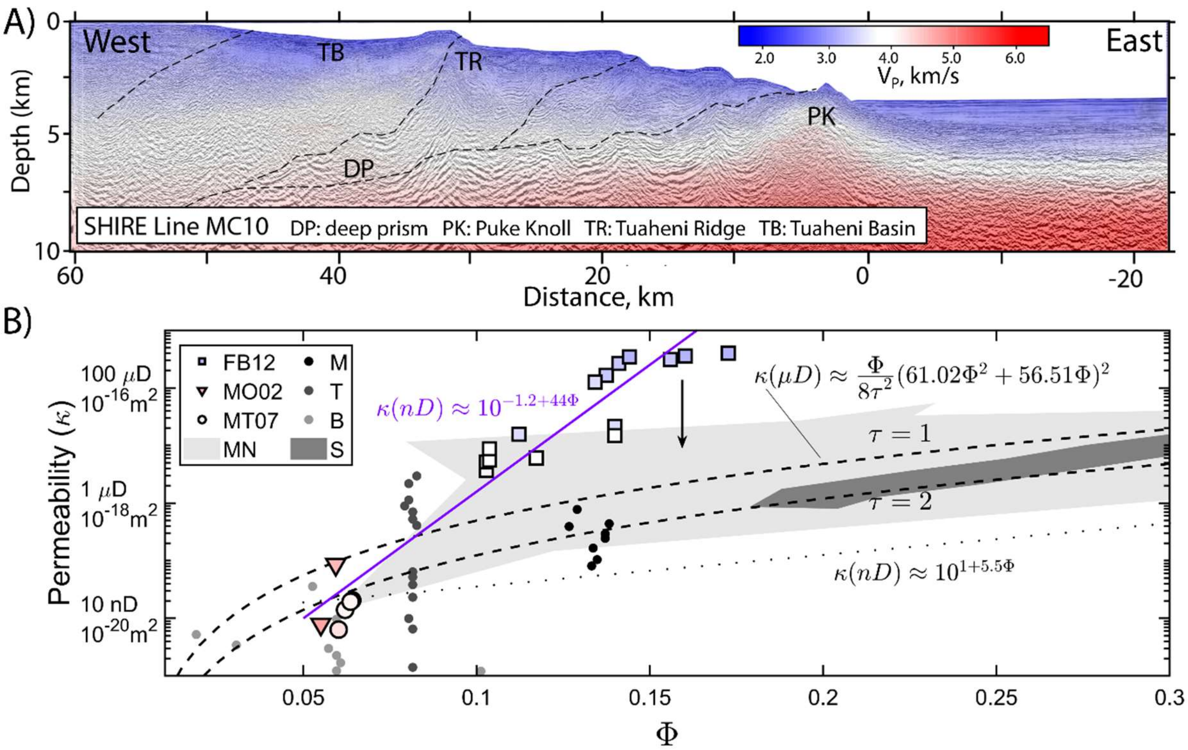

Figure 4. A) Velocity model along the SHIRE Line MC10 (Gase et al., 2021). B) Summary of laboratory results: permeabilities vs porosity and color-coded markers (colorbar in panel A) as a function of ultrasonic Vp for samples FB12, MO02, and MT07 (Tables S1,S2). The arrow indicates how permeability varies when tests are performed using water rather than helium gas. Dashed lines indicate eq. 3 permeability vs porosity model. The dotted line represents an average permeability for unconsolidated clays and possibly a lower bound for the permeability of HM sediments (eq. 1, Neuzil, 1994). S data (dark-gray area) are for siltstones (Reece et al., 2012). The continuous line (eq. 2) fits our data and agrees with measured mudrock permeabilities indicated by the MN gray-shaded area (Magara, 1978; Neglia, 1979). Such a line also represents an upper bound for the permeability of HM rocks. M, T, and B data are permeabilities measured in boreholes (M: Reisdorf et al. (2016), Yu et al. (2017); T: Boisson et al. (2001); B: Intera Eng. Ltd. (2011), Roberts et al. (2011), Walsh (2011)).

Our sample permeabilities range from 1 nD to 1 mD, with the samples representing the deep part of the prism being the tightest. Neuzil (1994, 2019) compiled data from several studies on unconsolidated clays with a maximum porosity of 80%, and consolidated mudrocks with porosities <35%. Saffer & Bekins (1998) followed Neuzil's work and described the permeability (κ) of the Nankai accretionary complex as:

$$\boldsymbol{\kappa(nD) \approx 10^{1+5.5\phi}} \qquad \text{eq.1}$$

which fits the porosity-permeability relationship of unconsolidated sediments and is a lower bound for the permeability of mudrocks similar to our samples (Magara, 1978; Neglia, 1979; Reece et al., 2012). On the other hand, we found that:

$$\boldsymbol{\kappa}(\boldsymbol{nD}) \approx \mathbf{10}^{-\mathbf{1.2}+\mathbf{44}\boldsymbol{\phi}} \qquad \text{eq.2}$$

fits our results and is an upper bound for the permeability of mudrocks. We suggest that equation 2 (Fig 4B) overestimate permeabilities in the Northern Hikurangi accretionary prism at depths >1 km because helium gas is not as efficient as seawater in activating swelling clays, whose expansion lowers the effective permeabilities (Villar et al., 2005); At burial depths >1-2 km, the porosity of clay-bearing sediments and mudrocks drops below 35% (Griffiths & Joshi, 1989; Magara, 1978; Skempton, 1969). Permeabilities measured in boreholes are typically orders of magnitude higher than those measured in the laboratory due to the presence of fractures (Fig 4B lines M,T,B) (Neuzil, 2019), and numerical models of permeability in microfractured claystones agree with the mudrocks porosity-permeability in Fig 4B (Vora & Dugan, 2019). Therefore, we propose that the permeability of mudrocks, similar to those the Northern Hikurangi accretionary prism, can be described by a Kozeny-Carman relation (dashed lines in Fig 4B):

$$\boldsymbol{\kappa} = \frac{\boldsymbol{\phi}}{\mathbf{8}\boldsymbol{\tau}^{\mathbf{2}}}\boldsymbol{R}^{\mathbf{2}} \qquad \text{eq.3}$$

Where $\boldsymbol{\tau}$ is tortuosity, and *R* is the median pore diameter (Carman, 1997). We obtained $\boldsymbol{R}(\boldsymbol{nm}) = \mathbf{61.02}\boldsymbol{\phi}^{\mathbf{2}} + \mathbf{56.51}\boldsymbol{\phi}$ from data reported by Hunt (1996) for mudrocks.

Every 1-2 years, the northern HM experiences an SSE that lasts several weeks (Wallace, 2020). Recent analyses of the APG data offshore Gisborne have shown that the 2014 SSE may have experienced up to 30 cm of slip in the center of a ~100 km wide patch, though less displacement is expected along the edges (Yohler et al., 2019). Some authors have suggested that SSEs that originate along the decollement at the base of the wedge are accompanied by slip diverted to thrust faults in the Hikurangi accretionary wedge (Shaddox & Schwartz, 2019). We expect SSEs to fracture the rocks, deform and cause granular flow along these thrust faults **(Chen, 2023; Fagereng et al., 2019; Morgan et al., 2022)**. Our pre and post-failure laboratory measurements suggest that these processes might increase the deeper prism permeability, where MT07 equivalent rocks may be present, by 2-3 orders of magnitude.

The fractured sample MT07 regained its pre-fracturing permeability over the course of several weeks. Between stages S1 and S2, the permeability recovery was achieved in dry conditions, possibly through visco-plastic deformation -also observed in sample FB12- and likely concentrated near soft minerals such as clays (Mondol et al., 2008). Between stages S2 and S3 (humidification), the permeability decreased by a factor of 5 while the fracture aperture increased, which could be explained by clay swelling, mineral softening, and dissolution and precipitation of carbonates **(Cadoret, 1993; Erguler & Ulusay, 2009; Galibert, 2016; Vanorio et al., 2008)**. Once confined, softened minerals and hydrated clays deform and clog the fracture more efficiently than dry minerals, explaining the permeability loss. Further investigating the permeability loss in rock samples is beyond the scope of the paper, but we suggest that permeability healing also affects HM faults especially above the 5-7 km deep temperature-controlled smectite-illite transition (Antriasian et al., 2018; Freed & Peacor, 1989; Pecher et al., 2017; Tisato & Marelli, 2013).

In the Hikurangi subduction zone, fluids expelled from pore space and fluids released by dehydration reactions travel along the plate interface or through the accretionary wedge (Ellis et al., 2015). As the fluid pressure increases near the decollement and inside the accretionary wedge, conditions may become favorable for an SSE (Burgreen-Chan et al., 2016; Kobayashi & Sato, 2021). Though this mechanism has been proposed for several subduction zones where SSE occur at larger depths (Audet et al., 2009; Kodaira et al., 2004), the analysis of Warren-Smith et al. (2019) on the northern HM, is also compatible with the sealing of fluid pathways after an SSE. The expansion and plastic deformation of clays may provide an efficient mechanism to reduce permeability over weeks or months after an SSE.

Shreedharan et al. (2023) studied sediments collected above the décollement of the Hikurangi margin, showing that their strength recovers little after shear testing. Minimal shear strength recovery is conducive to SSEs because it limits the accumulation of elastic energy from tectonic forces. Post-SSE permeability healing controls the development and recovery of pre-SSE overpressures, which together with a low mechanical strength, will set favorable conditions for a new SSE.

5 Conclusions

We provided relationships between porosity, permeability, and confining pressure for rocks that make up the accretionary prism of the northern HM. We suggest an empirical porosity-permeability relationship (eq. 3) to model fluid transport and estimate effective stress in shallow subduction zones. Mechanical failure of siltstones enhances permeability, but for several weeks, healing reduces the permeability again, suggesting that after an SSE, sediments deep in the northern HM accretionary prism can recover permeability efficiently within the time frame of an SSE as a mechanism explaining the regular recurrence of these events.

Acknowledgments

We thank editor Lucy Flesh, and reviewers Carolyn Boulton, Ake Fagereng, and one anonymous, Luc Lavier and Dominic Strogen for discussions. NSF supported this research (OCE-1949171).

Open Research

Analytical data are publicly available at https://doi.org/10.18738/T8/RMXMIQ.

References

Adams, C. J., & Graham, I. J. (1996). Metamorphic and tectonic geochronology of the Torlesse Terrane, Wellington, New Zealand. *New Zealand Journal of Geology and Geophysics*, *39*(2), 157–180. https://doi.org/10.1080/00288306.1996.9514703

Antriasian, A., Harris, R. N., Tréhu, A. M., Henrys, S. A., Phrampus, B. J., Lauer, R., et al. (2018). Thermal Regime of the Northern Hikurangi Margin, New Zealand. *Geophysical Journal International*. https://doi.org/10.1093/gji/ggy450

Aretusini, S., Meneghini, F., Spagnuolo, E., Harbord, C. W., & Di Toro, G. (2021). Fluid pressurisation and earthquake propagation in the Hikurangi subduction zone. *Nature Communications*, *12*(1), 2481. https://doi.org/10.1038/s41467-021-22805-w

Audet, P., Bostock, M. G., Christensen, N. I., & Peacock, S. M. (2009). Seismic evidence for overpressured subducted oceanic crust and megathrust fault sealing. *Nature*, *457*, 76–78. https://doi.org/10.1038/nature07650

Bangs, N. L., Morgan, J. K., Bell, R. E., Han, S., Arai, R., Gase, A. C., et al. (2023). Slow slip along the Hikurangi margin linked to fluid-rich sediments trailing subducting seamounts. *Nature Geoscience*, *IN PRESS*.

Barnes, P. M., Wallace, L. M., Saffer, D. M., Bell, R. E., Underwood, M. B., Fagereng, A., et al. (2020). Slow slip source characterized by lithological and geometric heterogeneity. *Science Advances*, *6*(13). https://doi.org/10.1126/sciadv.aay3314

Bassett, D., Arnulf, A., Henrys, S., Barker, D., Avendonk, H., Bangs, N., et al. (2022). Crustal Structure of the Hikurangi Margin From SHIRE Seismic Data and the Relationship Between Forearc Structure and Shallow Megathrust Slip Behavior. *Geophysical Research Letters*, *49*(2). https://doi.org/10.1029/2021GL096960

Bell, R., Sutherland, R., Barker, D. H. N., Henrys, S., Bannister, S., Wallace, L., & Beavan, J. (2010). Seismic reflection character of the Hikurangi subduction interface, New Zealand, in the region of repeated Gisborne slow slip events. *GJI*, *180*, 34–48. https://doi.org/10.1111/j.1365-246X.2009.04401.x

Birch, F. (1960). The velocity of compressional waves in rocks to 10 kilobars: 1. *Journal of Geophysical Research*, *65*(4), 1083–1102. https://doi.org/10.1029/JZ065i004p01083

Bland, K. J., Uruski, C. I., & Isaac, M. J. (2015). Pegasus Basin, eastern New Zealand: A stratigraphic record of subsidence and subduction, ancient and modern. *NZJGG*, *58*, 319–343. https://doi.org/10.1080/00288306.2015.1076862

Boisson, J.-Y., Bertrand, L., Heitz, J.-F., & Golvan, Y. (2001). In situ and laboratory investigations of fluid flow through an argillaceous formation at different scales of space and time, Tournemire tunnel, southern France. *Hydrogeology Journal*, *9*(1), 108–123. https://doi.org/10.1007/s100400000119

Boulton, C., Niemeijer, A. R., Hollis, C. J., Townend, J., Raven, M. D., Kulhanek, D. K., & Shepherd, C. L. (2019). Temperature-dependent frictional properties of heterogeneous Hikurangi Subduction Zone input sediments, ODP Site 1124. *Tectonophysics*, *757*, 123–139. https://doi.org/10.1016/j.tecto.2019.02.006

Boulton, C., Mizera, M., Niemeijer, A. R., Little, T. A., Müller, I. A., Ziegler, M., & Hamers, M. F. (2022). Observational and theoretical evidence for frictional-viscous flow at shallow crustal levels. *Lithos*, *428–429*, 106831. https://doi.org/10.1016/j.lithos.2022.106831

Burgreen-Chan, B., Meisling, K. E., & Graham, S. (2016). Basin and petroleum system modelling of the East Coast Basin, New Zealand: a test of overpressure scenarios in a convergent margin. *Basin Research*, *28*(4), 536–567. https://doi.org/10.1111/bre.12121

Cadoret, T. (1993). *Effet de la saturation eau-gaz sur les proprietes acoustiques des roches* (PhD Thesis). Université Paris Diderot - Paris 7., Paris. Retrieved from http://www.theses.fr/1993PA077130

Carman, P. C. (1997). Fluid flow through granular beds. *Chemical Engineering Research and Design*, *75*, S32–S48. https://doi.org/10.1016/S0263-8762(97)80003-2

Chen, J. (2023). The Emergence of Four Types of Slow Slip Cycles on Dilatant, Fluid Saturated Faults. *Journal of Geophysical Research: Solid Earth*, *128*(2), e2022JB024382. https://doi.org/10.1029/2022JB024382

Dutilleul, J., Bourlange, S., & Géraud, Y. (2021). Porosity and compaction state at the active Pāpaku thrust fault in the frontal accretionary wedge of the north Hikurangi margin. *G3*, *22*, e2020GC009325. https://doi.org/10.1029/2020GC009325

Dvorkin, J., & Nur, A. (1996). Elasticity of high-porosity sandstones: Theory for two North Sea data sets. *GEOPHYSICS*, *61*(5), 1363–1370. https://doi.org/10.1190/1.1444059

Eberhart-Phillips, D., Han, D.-H., & Zoback, M. D. (1989). Empirical relationships among seismic velocity, effective pressure, porosity, and clay content in sandstone. *GEOPHYSICS*, *54*(1), 82–89. https://doi.org/10.1190/1.1442580

Ellis, S., Fagereng, Å., Barker, D., Henrys, S., Saffer, D., Wallace, L., et al. (2015). Fluid budgets along the northern Hikurangi subduction margin, New Zealand: the effect of a subducting seamount on fluid pressure. *GJI*, *202*, 277–297. https://doi.org/10.1093/gji/ggv127

Erguler, Z. A., & Ulusay, R. (2009). Water-induced variations in mechanical properties of clay-bearing rocks. *International Journal of Rock Mechanics and Mining Sciences*, *46*(2), 355–370. https://doi.org/10.1016/j.ijrmms.2008.07.002

Fagereng, Å., Savage, H. M., Morgan, J. K., Wang, M., Meneghini, F., Barnes, P. M., et al. (2019). Mixed deformation styles observed on a shallow subduction thrust, Hikurangi margin, New Zealand. *Geology*, *47*, 872–876. https://doi.org/10.1130/G46367.1

Freed, R. L., & Peacor, D. R. (1989). Variability in temperature of the smectite/illite reaction in Gulf Coast sediments. *Clay Minerals*, *24*(2), 171–180. https://doi.org/10.1180/claymin.1989.024.2.05

French, M. E., & Morgan, J. K. (2020). Pore Fluid Pressures and Strength Contrasts Maintain Frontal Fault Activity, Northern Hikurangi Margin, New Zealand. *GRL*, *47*, e2020GL089209. https://doi.org/10.1029/2020GL089209

Galibert, P. (2016). Quantitative estimation of water storage and residence time in the epikarst with time-lapse refraction seismic. *Geophysical Prospecting*, *64*(2), 431–444. https://doi.org/10.1111/1365-2478.12272

Gase, A. C., Van Avendonk, H. J. A., Bangs, N. L., Bassett, D., Henrys, S. A., Barker, D. H. N., et al. (2021). Crustal Structure of the Northern Hikurangi Margin, New Zealand: Variable Accretion and Overthrusting Plate Strength Influenced by Rough Subduction. *Journal of Geophysical Research: Solid Earth*, *126*(5), e2020JB021176. https://doi.org/10.1029/2020JB021176

Gassmann, F. (1951). Elastic waves through a packing of spheres. *GEOPHYSICS*, *16*(4), 673–685. https://doi.org/10.1190/1.1437718

Griffiths, F. J., & Joshi, R. C. (1989). Change in pore size distribution due to consolidation of clays. *Géotechnique*, *39*(1), 159–167. https://doi.org/10.1680/geot.1989.39.1.159

Hunt, J. M. (1996). *Petroleum geochemistry and geology* (2nd ed). New York: W.H. Freeman.

Im, K., Saffer, D., Marone, C., & Avouac, J. P. (2020). Slip-rate-dependent friction as a universal mechanism for slow slip events. *Nature Geoscience*, *13*(10). https://doi.org/10.1038/s41561-020-0627-9

Intera Eng. Ltd. (2011). *Descriptive Geosphere Site Model*. 2011: Intera Eng. Ltd.

Kitajima, H., & Saffer, D. M. (2012). Elevated pore pressure and anomalously low stress in regions of low frequency earthquakes along the Nankai Trough subduction megathrust: LOW STRESS AT LOW SEISMIC VELOCITY ZONE. *Geophysical Research Letters*, *39*(23), n/a-n/a. https://doi.org/10.1029/2012GL053793

Kobayashi, T., & Sato, T. (2021). Estimating Effective Normal Stress During Slow Slip Events From Slip Velocities and Shear Stress Variations. *Geophysical Research Letters*, *48*(20). https://doi.org/10.1029/2021GL095690

Kodaira, S., Iidaka, T., Kato, A., Park, J.-O., Iwasaki, T., & Kaneda, Y. (2004). High pore fluid pressure may cause silent slip in the Nankai Trough. *Science*, *304*, 1295–1298.

van de Lagemaat, S. H. A., Mering, J. A., & Kamp, P. J. J. (2022). Geochemistry of syntectonic carbonate veins within Late Cretaceous turbidites, Hikurangi margin (New Zealand): Implications for a mid-Oligocene age of subduction initiation. *G3*, *23*, e2021GC010125. https://doi.org/10.1029/2021GC010125

Leah, H., Fagereng, Å., Bastow, I., Bell, R., Lane, V., Henrys, S., et al. (2022). The northern Hikurangi margin three-dimensional plate interface in New Zealand remains rough 100 km from the trench. *Geology*, *50*, 1256–1260. https://doi.org/10.1130/G50272.1

Liu, H.-P., Anderson, D. L., & Kanamori, H. (1976). Velocity dispersion due to anelasticity; implications for seismology and mantle composition. *Geophysical Journal International*, *47*(1), 41–58. https://doi.org/10.1111/j.1365-246X.1976.tb01261.x

Magara, K. (1978). *Compaction and fluid migration: practical petroleum geology*. Amsterdam, New York: Elsevier Scientific Pub. Co. ; Distributors for the U.S. and Can., Elsevier North-Holland.

Mazengarb, C., & Speden, I. G. (2000). Geology of the Raukumara area. geological map 6 60 p. + 1 fold. map, Lower Hutt: Institute of Geological & Nuclear Sciences.

Mondol, N. H., Bjørlykke, K., & Jahren, J. (2008). Experimental compaction of clays: relationship between permeability and petrophysical properties in mudstones. *Petroleum Geoscience*, *14*(4), 319–337. https://doi.org/10.1144/1354-079308-773

Morgan, J. K., Solomon, E. A., Fagereng, A., Savage, H. M., Wang, M., Meneghini, F., et al. (2022). Seafloor overthrusting causes ductile fault deformation and fault sealing along the Northern Hikurangi Margin. *Earth and Planetary Science Letters*, *593*, 117651. https://doi.org/10.1016/j.epsl.2022.117651

Mortimer, N., Rattenbury, M., King, P., Bland, K., Barrell, D., Bache, F., et al. (2014). High-level stratigraphic scheme for New Zealand rocks. *New Zealand Journal of Geology and Geophysics*, *57*(4), 402–419. https://doi.org/10.1080/00288306.2014.946062

Neglia, S. (1979). Migration of Fluids in Sedimentary Basins1. *AAPG Bulletin*, *63*(4), 573–597. https://doi.org/10.1306/2F918194-16CE-11D7-8645000102C1865D

Neuzil, C. E. (1994). How permeable are clays and shales? *Water Resources Research*, *30*(2), 145–150. https://doi.org/10.1029/93WR02930

Neuzil, C. E. (2019). Permeability of Clays and Shales. *Annual Review of Earth and Planetary Sciences*, *47*(1), 247–273. https://doi.org/10.1146/annurev-earth-053018-060437

Nicol, A., Mazengarb, C., Chanier, F., Rait, G., Uruski, C., & Wallace, L. (2007). Tectonic evolution of the active Hikurangi subduction margin, New Zealand, since the Oligocene: HIKURANGI SUBDUCTION MARGIN TECTONICS. *Tectonics*, *26*(4), n/a-n/a. https://doi.org/10.1029/2006TC002090

Passarelli, L., Selvadurai, P. A., Rivalta, E., & Jónsson, S. (2021). The source scaling and seismic productivity of slow slip transients. *Science Advances*, *7*(32), eabg9718. https://doi.org/10.1126/sciadv.abg9718

Pecher, I. A., Villinger, H., Kaul, N., Crutchley, G. J., Mountjoy, J. J., Huhn, K., et al. (2017). A Fluid Pulse on the Hikurangi Subduction Margin: Evidence From a Heat Flux Transect Across the Upper Limit of Gas Hydrate Stability. *Geophysical Research Letters*, *44*(24). https://doi.org/10.1002/2017GL076368

Rabinowitz, H. S., Savage, H. M., Skarbek, R. M., Ikari, M. J., Carpenter, B. M., & Collettini, C. (2018). Frictional behavior of input sediments to the Hikurangi trench, New Zealand. *G3*, *19*, 2973–2990. https://doi.org/10.1029/2018GC007633

Reece, J. S., Flemings, P. B., Dugan, B., Long, H., & Germaine, J. T. (2012). Permeability-porosity relationships of shallow mudstones in the Ursa Basin, northern deepwater Gulf of Mexico: MUDSTONE PERMEABILITY-POROSITY BEHAVIOR. *Journal of Geophysical Research: Solid Earth*, *117*(B12), n/a-n/a. https://doi.org/10.1029/2012JB009438

Reisdorf, A. G., Hostettler, B., Jaeggi, D., Deplazes, G., Blaesi, H., Morard, A., et al. (2016). Litho- and biostratigraphy of the 250 m-deep Mont Terri BDB-1 borehole through the Opalinus Clay and bounding formations, St Ursanne, Switzerland. https://doi.org/10.13140/RG.2.2.15045.04322

Roberts, R., Chace, D., Beauheim, R., & Avis, J. (2011). *Analysis of straddle-packer tests in DGR boreholes* (Technical report No. TR-08-32). Ottawa, Canada: Geofirma Eng. Ltd.

Saffer, D. M., & Bekins, B. A. (1998). Episodic fluid flow in the Nankai accretionary complex: Timescale, geochemistry, flow rates, and fluid budget. *Journal of Geophysical Research: Solid Earth*, *103*(B12), 30351–30370. https://doi.org/10.1029/98JB01983

Saffer, D. M., & Wallace, L. M. (2015). The frictional, hydrologic, metamorphic and thermal habitat of shallow slow earthquakes. *NG*, *8*, 594–600. https://doi.org/10.1038/ngeo2490

Saxena, N., & Mavko, G. (2014). Exact equations for fluid and solid substitution. *GEOPHYSICS*, *79*(3), L21–L32. https://doi.org/10.1190/geo2013-0187.1

Schwartz, S. Y., & Rokosky, J. M. (2007). Slow slip events and seismic tremor at circum-Pacific subduction zones. *RG*, *45*, RG3004. https://doi.org/10.1029/2006RG000208

Shaddox, H. R., & Schwartz, S. Y. (2019). Subducted seamount diverts shallow slow slip to the forearc of the northern Hikurangi subduction zone, New Zealand. *Geology*, *47*, 415–418. https://doi.org/10.1130/G45810.1

Shreedharan, S., Ikari, M., Wood, C., Saffer, D., Wallace, L., & Marone, C. (2022). Frictional and Lithological Controls on Shallow Slow Slip at the Northern Hikurangi Margin. *G3*, *23*, e2021GC010107. https://doi.org/10.1029/2021GC010107

Shreedharan, S., Saffer, D., Wallace, L. M., & Williams, C. (2023). Ultralow frictional healing explains recurring slow slip events. *Science*, *379*(6633), 712–717. https://doi.org/10.1126/science.adf4930

Skempton, A. W. (1969). The consolidation of clays by gravitational compaction. *Quarterly Journal of the Geological Society*, *125*(1–4), 373–411. https://doi.org/10.1144/gsjgs.125.1.0373

Sun, T., Saffer, D., & Ellis, S. (2020). Mechanical and hydrological effects of seamount subduction on megathrust stress and slip. *Nature Geoscience*, *13*(3), 249–255. https://doi.org/10.1038/s41561-020-0542-0

Sutherland, H. J., & Cave, S. P. (1980). Argon gas permeability of new mexico rock salt under hydrostatic compression. *International Journal of Rock Mechanics and Mining Sciences & Geomechanics Abstracts*, *17*(5), 281–288. https://doi.org/10.1016/0148-9062(80)90810-4

Tisato, N., & Marelli, S. (2013). Laboratory measurements of the longitudinal and transverse wave velocities of compacted bentonite as a function of water content, temperature, and confining pressure: ELASTIC PROPERTIES OF BENTONITE. *Journal of Geophysical Research: Solid Earth*, *118*(7), 3380–3393. https://doi.org/10.1002/jgrb.50252

Tisato, N., Madonna, C., & Saenger, E. H. (2021). Attenuation of Seismic Waves in Partially Saturated Berea Sandstone as a Function of Frequency and Confining Pressure. *Frontiers in Earth Science*, *9*, 641177. https://doi.org/10.3389/feart.2021.641177

Tsuji, T., & Iturrino, G. J. (2008). Velocity-porosity relationships in oceanic basalt from eastern flank of the Juan de Fuca Ridge: The effect of crack closure on seismic velocity. *Exploration Geophysics*, *39*(1), 41–51. https://doi.org/10.1071/EG08001

Tsuji, T., Tokuyama, H., Costa Pisani, P., & Moore, G. (2008). Effective stress and pore pressure in the Nankai accretionary prism off the Muroto Peninsula, southwestern Japan. *Journal of Geophysical Research*, *113*(B11), B11401. https://doi.org/10.1029/2007JB005002

Vanorio, T., Scotellaro, C., & Mavko, G. (2008). The effect of chemical and physical processes on the acoustic properties of carbonate rocks. *The Leading Edge*, *27*(8), 1040–1048. https://doi.org/10.1190/1.2967558

Villar, M. V., Martín, P. L., & Barcala, J. M. (2005). Modification of physical, mechanical and hydraulic properties of bentonite by thermo-hydraulic gradients. *Engineering Geology*, *81*(3), 284–297. https://doi.org/10.1016/j.enggeo.2005.06.012

Vora, H. B., & Dugan, B. (2019). Porosity-Permeability Relationships in Mudstone from Pore-Scale Fluid Flow Simulations using the Lattice Boltzmann Method. *Water Resources Research*, *55*(8), 7060–7071. https://doi.org/10.1029/2019WR024985

Wallace, Laura M. (2020). Slow Slip Events in New Zealand. *AREPS*, *48*, 175–203. https://doi.org/10.1146/annurev-earth-0717190055104

Wallace, L.M., Saffer, D. M., Barnes, P. M., Pecher, I. A., Petronotis, K. E., LeVay, L. J., & the Expedition 372/375 Scientists. (2019). *Hikurangi Subduction Margin Coring, Logging, and Observatories*. College Station, TX: Proceedings of the International Ocean Discovery Program, 372B/375. https://doi.org/10.14379/iodp.proc.372B375.102.2019

Walsh, R. (2011). *Compilation and consolidation of field and laboratory data for hydrogeological properties* (DGR Site Charact. Doc. No. TR-08-10). Ottawa, Canada: Geofirma Eng. Ltd.

Warren-Smith, E., Fry, B., Wallace, L., Chon, E., Henrys, S., Sheehan, A., et al. (2019). Episodic stress and fluid pressure cycling in subducting oceanic crust during slow slip. *Nature Geoscience*, *12*(6), 475–481. https://doi.org/10.1038/s41561-019-0367-x

Yohler, R., Bartlow, N., Wallace, L. M., & Williams, C. (2019). Time-Dependent Behavior of a Near-Trench Slow-Slip Event at the Hikurangi Subduction Zone. *Geochemistry, Geophysics, Geosystems*, *20*(8), 4292–4304. https://doi.org/10.1029/2019GC008229

Yu, C., Matray, J.-M., Gonçalvès, J., Jaeggi, D., Gräsle, W., Wieczorek, K., et al. (2017). Comparative study of methods to estimate hydraulic parameters in the hydraulically undisturbed Opalinus Clay (Switzerland). *Swiss Journal of Geosciences*, *110*(1), 85–104. https://doi.org/10.1007/s00015-016-0257-9

Permeability and elastic properties of rocks from the northern Hikurangi margin: Implications for slow-slip events

Nicola Tisato[1], Carolyn D. Bland[1*], Harm Van Avendonk[2], Nathan Bangs[2], Hector Garza[1], Omar Alamoudi[1], Kelly Olsen[2†], Andrew Gase[2‡]

[1] Department of Earth and Planetary Sciences, Jackson School of Geosciences, The University of Texas at Austin, Austin, TX, U.S.

[3] Institute for Geophysics, Jackson School of Geosciences, The University of Texas at Austin, Austin, TX, U.S.

[*] Now at: Pariveda Solutions, Dallas, TX, U.S.

[†] Now at: Descartes Labs, 1607 Paseo de Peralta, Suite B, Sante Fe, NM, U.S.

[‡] Now at: Geology Department, Western Washington University, Bellingham, WA, U.S.

Corresponding author: Nicola Tisato (nicola.tisato@jsg.utexas.edu)

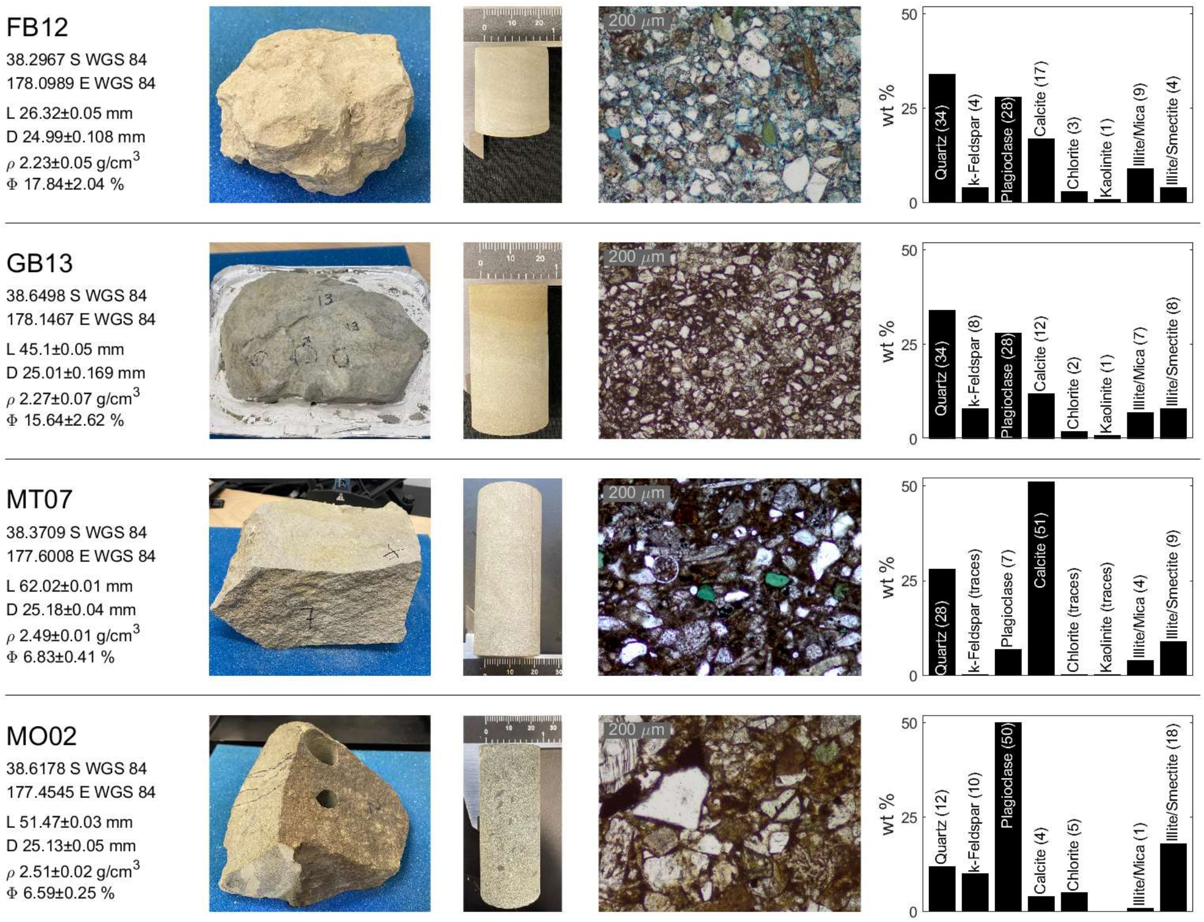

Figure S1. For each sample, the left column reports the geographic coordinates, length (L), diameter (D), density (ρ), and porosity (Φ). The three center columns are pictures of hand samples and transmitted light microphotographs. The right column reports mineral compositions according to X-ray diffraction analyses (XRD).

Sample preparation details

The end faces of each core plug were smoothed to parallel using a rock saw and a lathe equipped with an angular grinder. Parallelism was checked with a 0.01 mm resolution caliper. Each core was oven-dried at ~333 K for several days to reduce absorbed water. We then calculated the total volume and density of each core by measuring its mass and dimensions using a scale and a caliper to accuracies of 0.001 g and 0.02 mm, respectively. A helium pycnometer (Micromeritics AccuPyc II 1340) was used to measure the solid volume and porosity of each core.

To evenly distribute the saturating water or the helium gas to test permeability across the sample end-face, we placed 3.175 mm thickness, 10 μm grain size, AISI 316 stainless steel porous frits between each sample holder and the adjacent sample end-face.

Sample MT07 at stage S3 - i.e., fractured after being exposed to humidity - was epoxy impregnated before removing the rubber jacket to avoid offsetting the fracture.

Preparation of the saturating water for sample GB13

Water chemically equilibrated with sample GB13 was prepared and injected as follows: For several weeks before saturation, we submerged a few grams of GB13 granules in deionized water. Then, the injection of such aqueous fluid was performed using a high-pressure syringe pump (ISCO 260HP), recording – via a Matlab script - the injected volume and injection pressure. The latter was maintained constant to a value of 3 MPa lower than the confining pressure that varied between 20 and 50 MPa.

Ultrasonic and mechanical testing details

Testing was performed in the Rock Deformation Laboratory of UT Austin using a NER Autolab 1500 pressure vessel. Our samples have a maximum ultrasonic velocity of ~6 km/s and considering the testing frequency of 800 kHz, we estimated a maximum wavelength (λ_M) of 7.5 mm and, to avoid nearfield effects, we prepared cores with a length (L) > 3 λ_M. Velocities were estimated with the transmission method by measuring the time of travel of the elastic wave along the core plug (Birch, 1960). We corrected the first arrival by the delay introduced by the sample holders that was determined by a standard calibration procedure (e.g., Prelicz, 2005). A pulser-receiver apparatus (JSR Ultrasonics DPR300) generated a negative spike pulse with a typical duration of ~40 ns feeding the source ultrasonic transducer. We used a pulsing rate of 100 pulses/sec (PRF RATE=1), pulse amplitude of ~194 V (PULSE AMPLITUDE = 4, and PULSE ENERGY = HIGH Z 4), and damping of 331 Ohms (DAMPING = 1). In addition, the pulser-receiver produces a trigger signal (5 V in amplitude) to synchronize the pulser and the oscilloscope (Rigol DS1104Z-S) collecting the signals generated by the receiving transducer and amplified by the receiver. The latter has a gain of 66 dB (REL. GAIN = 79), a high-pass filter corner frequency of 1 MHz, and a low-pass filter corner frequency of 3 MHz. Two data transfer switches allow selecting the recording of the V_P, V_{S1} or V_{S2} signal. To improve the signal-to-noise ratio the oscilloscope collects and stacks 1024 signals and transmits the digitized wavelets to a computer via a USB port. Typically, the signal, comprising 1200 samples, is digitized every 0.2 μs or less and saved as a comma-separated-value (CSV) file. Shear velocities were calculated as the average of V_{S1} and V_{S2}.

All velocities (V) as a function of σ_M were fit according to Eberhart-Phillips et al., 1989:

$$V = a + k\,\sigma_M - b\,e^{-d\,\sigma_M} \qquad \text{eq. S1}$$

Where a, k, b, and d are fitting parameters. Table S1 reports the fitting parameters for all the measurements reported in Figure 2A. As σ_M increases, especially above ~50 MPa, the effect of the non-linear part of eq. S1 decreases, and V tends to be equal to:

$$V = a + k\,\sigma_M \qquad \text{eq. S2}$$

The exponential increase of velocity (e.g., $-b\,e^{-d\,\sigma_M}$) is controlled by crack closure (e.g., Eberhart-Phillips et al., 1989; Tsuji & Iturrino, 2008). Cracks are naturally occurring, but some of our sample cracks were probably produced during preparation. Therefore, the measured velocities and those modeled with eq. S1 possibly underestimate the velocities of the undisturbed rocks. On the other end, the velocities calculated according to eq. S2 represent an upper bound for the undisturbed rock velocities. Therefore, to provide a range of possible velocities, table S2 reports values calculated according to eqs. S1 and S2, and we used their average to color code the symbols in Figure 4B, which compares ultrasonic and seismic velocities in section MC10 (fig. 4A).

We compared the ultrasonic wave velocities of the saturated sample GB13 (wet) with the velocities calculated according to the Gassmann fluid substitution (Gassmann, 1951) as first-order comparison. We obtained the dry bulk and shear modulus from the measured ultrasonic velocities and density. We used a porosity of 15.64% and estimated the effective bulk modulus of the mineral material making up the rock (K_0=41.9 GPa) using the Voigt-Reuss-Hill average (Hill, 1952). Such an average was calculated considering the mineral abundances and bulk moduli in Table S3. The density of the water saturated sample (ρ_s) was calculated as:

$$\rho_s = \rho + \emptyset\, \rho_w \qquad \text{eq. S3}$$

Where ρ_w is the water density (1 g/cm^3).

Samples compaction was measured to 1 μm accuracy with a Linear Variable Displacement Transducer connected to the axial piston, whose signal was acquired along with the confining pressure and vertical force.

Sample	Vp a, km/s	Vp k, km/(s MPa)	Vp b, km/s	Vp d, 1/MPa	Vs a, km/s	Vs k, km/(s MPa)	Vs b, km/s	Vs d, 1/MPa
MT07	4.258817902	0.0004	0.550763843	0.015592476	2.287173194	0.0004	0.09790168	0.040302981
MO02	4.833190738	0.000477349	0.962464542	0.019981488	2.670892183	0.001066209	0.333323072	0.046859072
FB12	3.411081272	0.001491361	0.80796207	0.018920899	1.934911643	0.000515137	0.607538101	0.027957185
FB12 compacted	3.654526209	0.002210184	0.648879727	0.016973021	2.087187716	0.000481684	0.525301017	0.013531611
GB13 dry	3.197979485	0.0004	0.697908198	0.055000841	1.925084775	0.0004	0.37545229	0.053030252
GB13 wet	3.11957827	0.004527395	0.44414554	0.309940938	1.598263565	0.003703102	0.021526433	0.030134497

Table S1: Fitting parameters for the samples ultrasonic velocities according to eqs. S1 and S2.

Sample	Φ, %	κ, m2	σM, MPa	Vp (meas.) km/s	Vp (EP89) min, km/s	Vp (EP89) max, km/s	Vp (EP89) mean, km/s
FB12	17.3	3.95E-16	10	2.788	2.757	3.426	3.092
FB12	16.0	3.52E-16	20	2.937	2.887	3.441	3.164
FB12	15.6	3.04E-16	30	2.986	2.998	3.456	3.227
FB12	13.7	1.63E-16	50	3.055	3.172	3.486	3.329
FB12	13.4	1.24E-16	70	3.251	3.301	3.515	3.408
FB12	14.1	2.60E-16	30	2.968	2.998	3.456	3.227
FB12	14.4	3.38E-16	20	2.895	2.887	3.441	3.164
FB12 compacted	14.0	2.13E-17	30	3.333	3.331	3.721	3.526
FB12 compacted	14.0	1.46E-17	70	3.543	3.611	3.809	3.710
FB12 compacted	11.7	5.97E-18	150	3.866	3.935	3.986	3.961
FB12 compacted	10.3	3.64E-18	200	4.008	4.075	4.097	4.086
FB12 compacted	10.3	5.10E-18	150	3.863	3.935	3.986	3.961
FB12 compacted	10.4	5.56E-18	100	3.745	3.757	3.876	3.816
FB12 compacted	10.4	8.67E-18	70	3.618	3.611	3.809	3.710
FB12 compacted	11.2	1.54E-17	30	3.298	3.331	3.721	3.526
MO02	5.9	8.47E-20	30	4.353	4.320	4.848	4.584
MO02	5.5	7.80E-21	50	4.479	4.502	4.857	4.680
MT07	6.4	2.03E-20	30	3.838	3.926	4.271	4.098
MT07	6.2	1.39E-20	50	3.913	4.026	4.279	4.153
MT07	6.0	6.29E-21	70	3.995	4.102	4.287	4.194
MT07	6.4	1.92E-20	20	3.843	3.864	4.267	4.065

Table S2: Porosity, permeability, mean stress, and Vp for our sample data that are reported in Figure 4B. 'Vp (meas.)' indicate the measurements, 'Vp (EP89) min' is the velocity estimated using eq. S1, 'Vp (EP89) max' is the velocity estimated according to eq. S2. 'Vp

(EP89) mean' is the average between 'Vp (EP89) min' and 'Vp (EP89) max'. The latter is used to color-code the symbols of samples MT07, MO02, and FB12 in Figure 4B.

Mineral	Fraction	Bulk Modulus
Quartz	34%	37.0 GPa
K-feldspar	8%	37.5 GPa
Plagioclase	28%	76.0 GPa
Calcite	12%	77.0 GPa
Clays	18%	15.0 GPa

Table S3. Parameters used to calculate the effective bulk modulus of the minerals making up sample GB13 (K_0). Fractions are estimated from XRD (see Figure S1), and bulk moduli are taken from (Carmichael, 1989).

Permeability testing

Testing was performed in the Rock Deformation Laboratory of UT Austin using a NER Autolab 1500 pressure vessel. The two reservoirs connected to the sample end-faces have volumes V_1=58.725 ml and V_2=162.53 ml, and at the beginning of the test, we connected the reservoirs to a high-pressure helium gas bottle to raise their internal pressures to two different values $P_{1i} > P_{2i}$. While P_{1i} is greater than P_{2i}, helium flows through the sample until pressure equilibrium is reached. Two digital manometers (Keller LEO3) connected to a computer and a Matlab code record P1 and P2 over time (t). The two manometers also measure temperature (T). Permeability is then calculated as:

$$\kappa = -\frac{\beta\,\eta\,L}{\left(\frac{1}{V_1}+\frac{1}{V_2}\right) K\,A}, \qquad \text{eq. S4}$$

Where η and K are Helium viscosity and bulk modulus, respectively; L and A are the lengths and cross-section area of the sample; β is the exponent of the pressure decay:

$$P_1 = (P_{1i} - P_{2i})\, e^{\beta\, t} + P_f, \quad \text{eq. S5}$$

Where P_f is the equilibrium pressure, i.e., P_1 and P_2 at time infinite. We assume helium properties as a function of pressure and temperature from the national institute for standards and technology (NIST) fluid thermophysical properties (Arp et al., 1998; Ortiz-Vega et al., 2020). P_f and β were estimated by means of a non-linear least absolute residuals fit implemented in Matlab.

XRD and CT-scanner setup

Mineralogical X-ray diffraction analyses were conducted at the Geomaterials Characterization and Imaging Facility (GeoMatCl) at The University of Texas at Austin. Whole rock samples were manually homogenized, ground, and sieved to a 250 µm mesh size. XRD analyses were performed using a Bruker D8 diffractometer instrument equipped with Cu Kα radiation and a nickel filter, along with a LYNXEYE solid-state detector. The analyses were carried out at a voltage of 45 kV and a current of 40 mA, employing a 2θscan axis ranging from 3° to 70°, with step increments of .0195° (2θ) and a duration of 1 s per step. Whole rock X-ray patterns (Fig S2) were determined through Rietveld refinement utilizing Bruker TOPAS 4.2 software.

For clay speciation analyses (Fig S3), we followed the modified methods based on Hillier (2000) and Moore & Reynolds (1997). $CaCO_3$ rich samples were subjected to a modified HCl-

Na_2CO_2 treatment (5% diluted HCl) to disseminate clay minerals following the method of Komadel et al. (1990) and Meredith E. Ostrom (1961). Our study acknowledges that previous research has indicated instances where the utilization of HCl may not be optimal in clay X-ray diffraction (XRD) analyses due to the potential dissolution of clay minerals (Kumar et al., 2013; Hu et al., 2022). However, in the specific context of this study, the application of HCl was deemed necessary to mitigate the substantial presence of calcium carbonate (CaCO3). High concentrations of CaCO3 can overshadow clay minerals, rendering their interpretation impossible.

Disaggregated material was separated into a <2-micron clay fraction suspension using sodium hexametaphosphate, enabling the acquisition of clay speciation by excluding heavier non-phyllosilicate minerals. The <2-micron clay suspension was vacuum-filtered through a millipore filter and subsequently oriented onto a glass slide. The oriented clay mounts were subjected to ethylene glycol vapors for 24 hours, followed by heating (1 hour) to 400°C to identify swelling clays. Clay speciation X-ray patterns with a 2θ scan axis ranging from 3° to 70°, with step increments of 0.195° (2θ) and a duration of 1 s per step were evaluated using reference intensity ratios (RIR), and mineral intensity factors (MIF) with the MDI Jade software.

For CT-scanning we used an NSI scanner equipped with a Fein Focus High Power source, at 120 kV voltage and 0.14 mA current. CT scans were acquired at 33.3 µm per voxel resolution. The X-ray source was filtered using aluminum foil. The CT scanner is equipped with a Perkin Elmer detector, with 0.5 pF gain, and the 1800 projections were collected at 1 fps and 1x1 binning. The source-to-object distance was 150.566 mm, and the source to detector 963.799 mm. We performed a continuous CT scan by averaging 2 frames and by skipping 0 frames. We applied a beam-hardening correction of 0.25 and a post-reconstruction ring correction using the following parameters: oversample = 2, radial bin width = 21, sectors = 32, minimum arc length = 2, angular bin width = 9, angular screening factor = 4. The final reconstructed volume had a voxel size of 33.3 µm and 1873 slices.

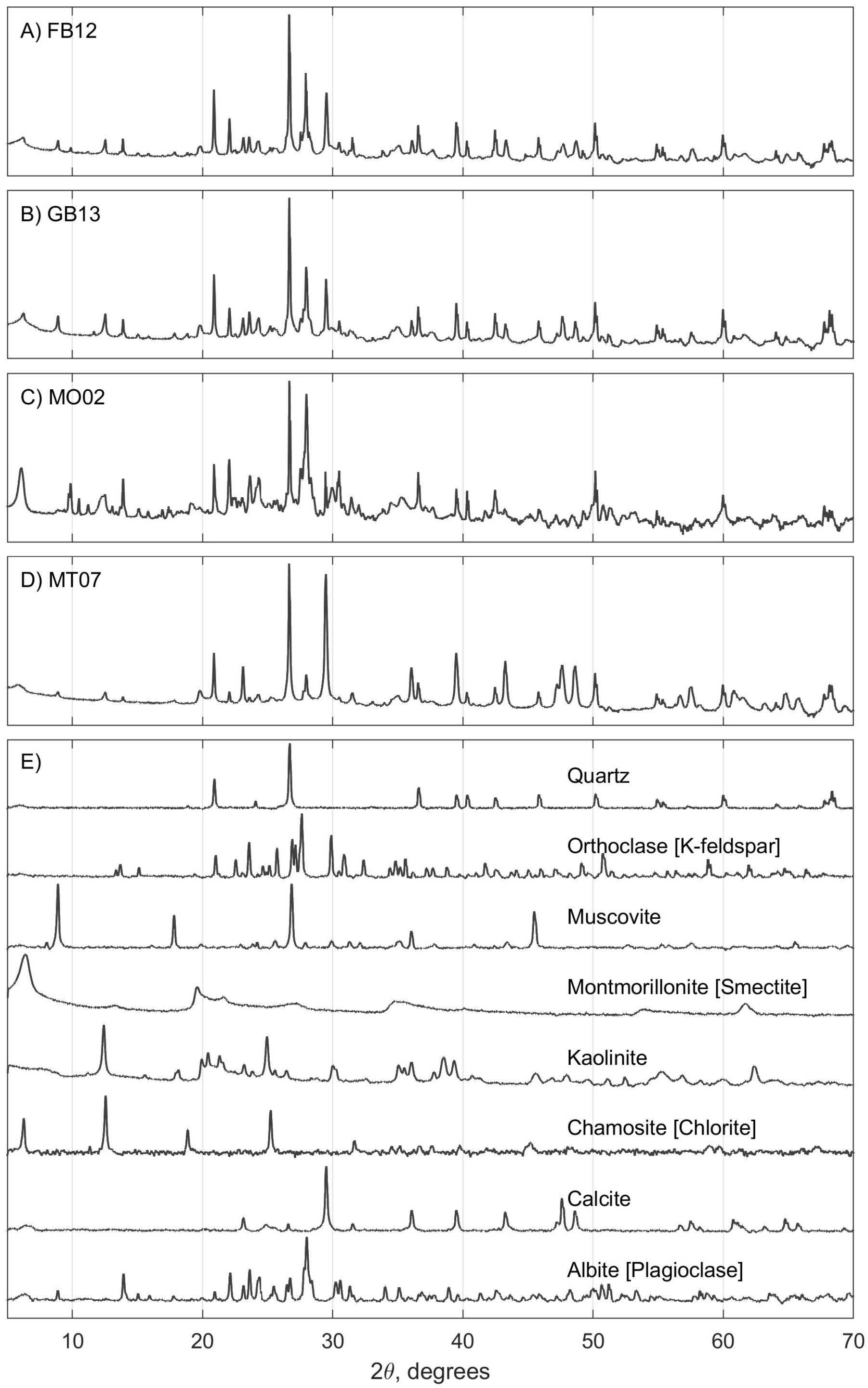

Figure S2. A-D) XRD spectra of the four samples. E) Standard spectra for the mineral comprising our samples. Data have been taken from the RRUFF database (Lafuente et al., 2015): Talc URL=rruff.info/R040137; Quartz URL=rruff.info/R040031; Orthoclase URL=rruff.info/R040055; Muscovite URL=rruff.info/R040104; Montmorillonite URL=rruff.info/R110052; Kaolinite URL=rruff.info/R140004; Chamosite URL=rruff.info/R060188; Calcite URL=rruff.info/R040070; Albite URL=rruff.info/R040068.

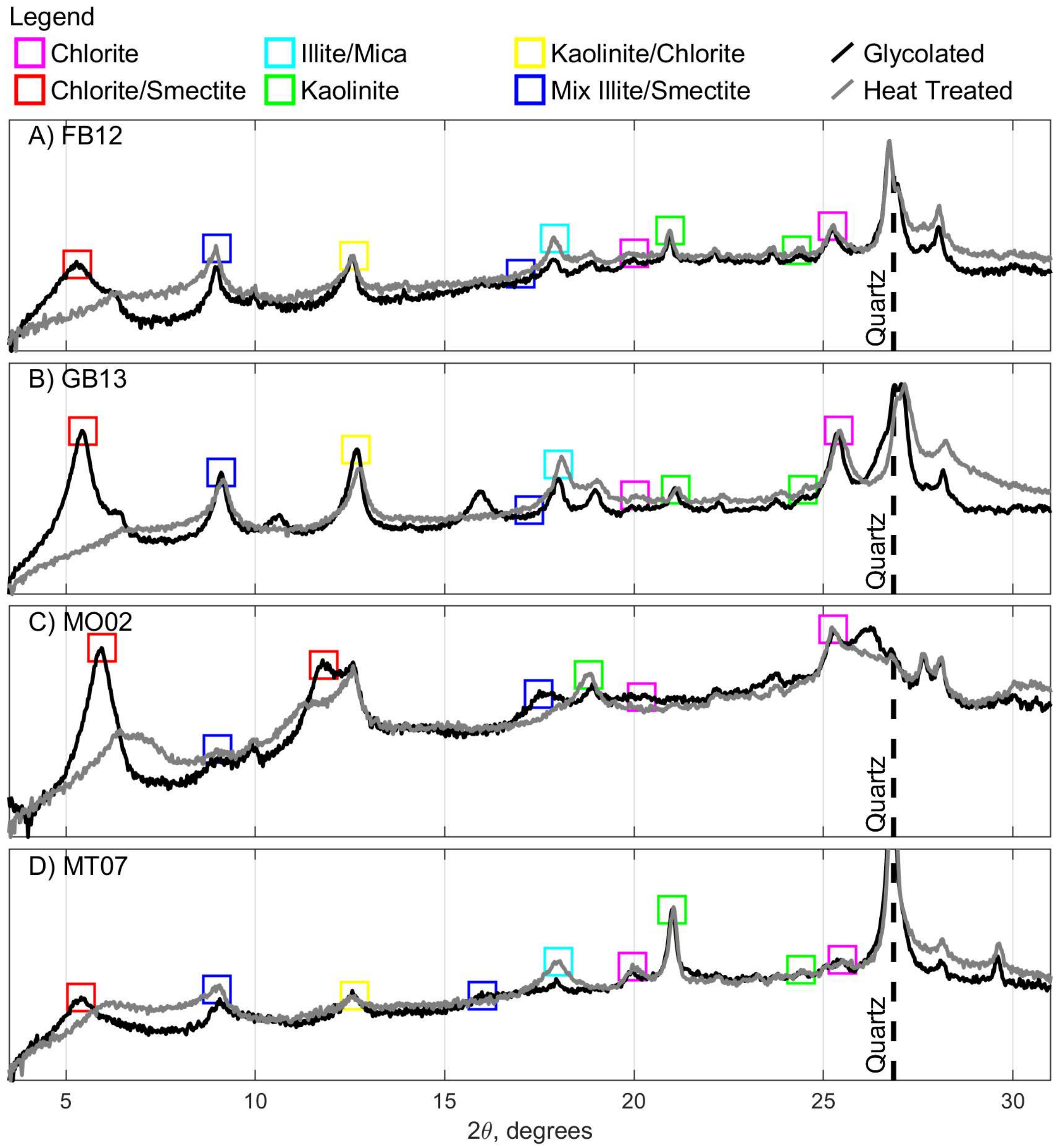

Figure S3. XRD clay patterns (oriented, glycolated, heat-treated at 400°C) for Illite/Mica, Mix Illite/Smectite, Kaolinite, and Chlorite minerals. Squares indicate peaks and portions of spectra used to speciate and estimate clay fractions for each sample.
A) Sample FB12 is dominated by Illite/Mica, followed by Mix Illite/Smectite, with minor quantities of Chlorite and Kaolinite. B) Sample GB13 exhibits an abundance of Mix Illite/Smectite and Illite/Mica, along with trace amounts of Chlorite and Kaolinite. C) Sample MO02 is notably rich in Mix Illite/Smectite, with a significant presence of Chlorite and minor content of Illite/Mica. D) Sample MT07 is primarily rich in Mix Illite/Smectite, featuring a notable abundance of Illite/Mica, and minor quantities of Chlorite and Kaolinite.

Fracture aperture calculation

To normalize CT-scan datasets, we fit a Gaussian function to the distribution of CT numbers to obtain a CT-number mean (m_x) and standard deviation (s_x), where x is either S1, S2, or S3. To compare datasets acquired at different stages, we created shifted images by shifting the CT-numbers of datasets S2 and S3 by m_{S1}-m_{S2} and m_{S1}-m_{S3}, respectively. We added a value of 1 to each voxel, cropped each image to 718x718 pixels around the sample center, and assigned a value of 0 to pixels with a distance >718/2 from the sample center. We binarized the datasets to assign each voxel to either solid rock or air by applying a threshold calculated as:

$$t_x = m_x - 2.5\ s_x \qquad \text{eq. S6}$$

The threshold was chosen equal to 2.5 times the standard deviation of the Gaussian fit because such a value marks the departure of the CT-number distributions from the Gaussian fit, suggesting that the fits model the voxels representing the rock (Figure S4). Voxels with CT-number equal to or greater than t_x were then assumed to represent rock and assigned a value of 255. Voxels with CT-number lower than t_x and greater than zero were assumed to be air and assigned a value of 128.

To obtain a FADP of a binarized dataset, we calculated: 1) The Euclidian distance of each voxel in the fracture. This is achieved by a) performing an iterative image morphological erosion assigning approximated distances of each fracture voxel from the fracture rim, and b) calculating the Euclidian distance of each voxel within the fracture from the closest voxel representing rock; 2) The skeleton of the fracture (SK) comprises the voxels that are within the fracture and have the maximum Euclidian distance from the fracture rim into respect the 26 surrounding voxels. Such a device extracts the center surface while preserving the topology and Euler number, also known as the Euler characteristic of the objects (Kerschnitzki et al., 2013; Lee et al., 1994). Finally, the FADP was calculated at each SK location by doubling the Euclidian distance recorded in such voxels.

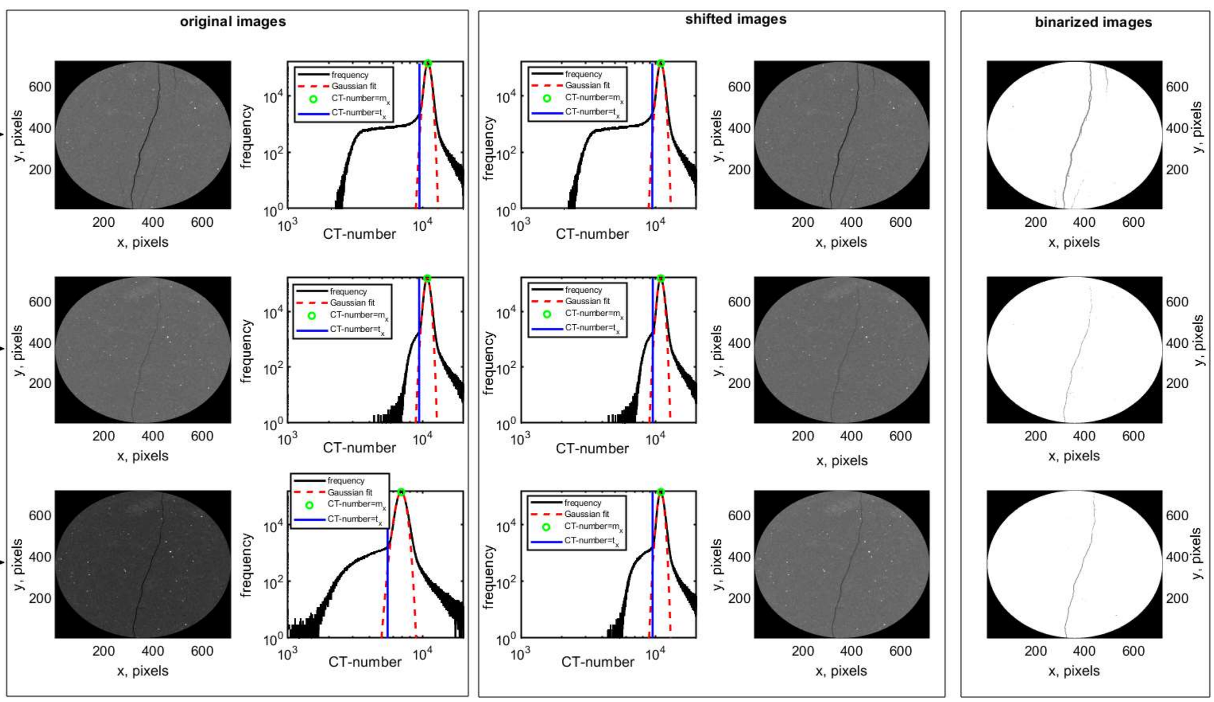

Figure S4. Image processing to normalize CT-scan datasets. An example of original CT images from the datasets (S1, S2 and S3) are shown in the first column. The second column reports the original datasets CT-number distributions, the Gaussian fits, the CT-number mean (m_x) and the threshold (t_x) (eq. S6). For dataset S1, columns three and four report the same chart and image shown in columns two and one, respectively. For S2 and S3, column three show the CT-number distributions of the shifted images, the Gaussian fits, m_x and t_x. Column 4 shows the shifted images for S2 and S3. Column five report three images of the binarized datasets.

References

Arp, V. D., McCarty, R. D., & Friend, D. G. (1998). *Thermophysical Properties of Helium-4 from 0.8 to 1500 K with Pressures to 2000 MPa* (Technical Report No. 1334 (revised)). NIST.

Birch, F. (1960). The velocity of compressional waves in rocks to 10 kilobars: 1. *Journal of Geophysical Research*, *65*(4), 1083–1102. https://doi.org/10.1029/JZ065i004p01083

Carmichael, R. S. (Ed.). (1989). *Practical handbook of physical properties of rocks and minerals*. Boca Raton, Fla: CRC Press.

Eberhart-Phillips, D., Han, D.-H., & Zoback, M. D. (1989). Empirical relationships among seismic velocity, effective pressure, porosity, and clay content in sandstone. *GEOPHYSICS*, *54*(1), 82–89. https://doi.org/10.1190/1.1442580

Gassmann, F. (1951). Elastic waves through a packing of spheres. *GEOPHYSICS*, *16*(4), 673–685. https://doi.org/10.1190/1.1437718

Hill, R. (1952). The Elastic Behaviour of a Crystalline Aggregate. *Proceedings of the Physical Society. Section A*, *65*(5), 349–354. https://doi.org/10.1088/0370-1298/65/5/307

Hillier, S. (2000). Accurate quantitative analysis of clay and other minerals in sandstones by XRD: comparison of a Rietveld and a reference intensity ratio (RIR) method and the importance of sample preparation. *Clay Minerals*, *35*(1), 291–302. https://doi.org/10.1180/000985500546666

Hu, B., Zhang, C., & Zhang, X. (2022). The Effects of Hydrochloric Acid Pretreatment on Different Types of Clay Minerals. *Minerals*, *12*(9), 1167. https://doi.org/10.3390/min12091167

Kerschnitzki, M., Kollmannsberger, P., Burghammer, M., Duda, G. N., Weinkamer, R., Wagermaier, W., & Fratzl, P. (2013). Architecture of the osteocyte network correlates with bone material quality: OSTEOCYTE NETWORK ARCHITECTURE CORRELATES WITH BONE MATERIAL QUALITY. *Journal of Bone and Mineral Research*, *28*(8), 1837–1845. https://doi.org/10.1002/jbmr.1927

Komadel, P., Schmidt, D., Madejová, J., & Číčel, B. (1990). Alteration of smectites by treatments with hydrochloric acid and sodium carbonate solutions. *Applied Clay Science*, *5*(2), 113–122. https://doi.org/10.1016/0169-1317(90)90017-J

Kumar, S., Panda, A. K., & Singh, R. K. (2013). Preparation and characterization of acids and alkali treated kaolin clay. *Bulletin of Chemical Reaction Engineering & Catalysis*, *8*(1), 61-69.

Lafuente, B., Downs, R. T., Yang, H., & Stone, N. (2015). 1. The power of databases: The RRUFF project. In T. Armbruster & R. M. Danisi (Eds.), *Highlights in Mineralogical Crystallography* (pp. 1–30). DE GRUYTER. https://doi.org/10.1515/9783110417104-003

Lee, T. C., Kashyap, R. L., & Chu, C. N. (1994). Building Skeleton Models via 3-D Medial Surface Axis Thinning Algorithms. *CVGIP: Graphical Models and Image Processing*, *56*(6), 462–478. https://doi.org/10.1006/cgip.1994.1042

Meredith E. Ostrom (2). (1961). Separation of Clay Minerals from Carbonate Rocks by Using Acid. *SEPM Journal of Sedimentary Research*, *Vol. 31*. https://doi.org/10.1306/74D70B1E-2B21-11D7-8648000102C1865D

Moore, D. M., & Reynolds, R. C. (1997). *X-ray diffraction and the identification and analysis of clay minerals* (2nd ed). Oxford ; New York: Oxford University Press.

Ortiz-Vega, D., Hall, K., Holste, J., Arp, V., Harvey, A., & Lemmon, E. (2020). Helmholtz equation of state for helium. *Journal of Physical and Chemical Reference Data*.

Prelicz, R. M. (2005). *Seismic anisotropy in peridotites from the Western Gneiss Region (Norway): laboratory measurements at high PT conditions and fabric based model predictions* [Application/pdf]. ETH Zurich. https://doi.org/10.3929/ETHZ-A-005115293

Tsuji, T., & Iturrino, G. J. (2008). Velocity-porosity relationships in oceanic basalt from eastern flank of the Juan de Fuca Ridge: The effect of crack closure on seismic velocity. *Exploration Geophysics*, *39*(1), 41–51. https://doi.org/10.1071/EG08001